Journal of Applied Polymer Science

WILEY

Applied Polymer SCIENCE

RESEARCH ARTICLE

Electromagnetic Interference Shielding Offered by Waterborne Poly(Urethane-Imide) Composites Reinforced With Carbon Nanostructures

Chih-Lung Lin[1,2] | Yen-Yu Cheng[1] | Syang-Peng Rwei[1]

[1]Institute of Organic and Polymeric Materials, National Taipei University of Technology, Taipei City, Taiwan | [2]The Kuroki Company, Limited, R&D Department, Tucheng District, Taiwan

Correspondence: Syang-Peng Rwei (f10714@ntut.edu.tw)

Received: 17 July 2024 | **Revised:** 11 December 2024 | **Accepted:** 28 December 2024

Funding: This work was supported by the National Science and Technology Council (112-2221-E-027-005-MY2).

ABSTRACT

Electromagnetic waves are produced in large volumes by the increasing number of electronic devices, and some devices must be shielded from these waves to prevent electromagnetic interference (EMI). Traditional metals are effective shielders but have limitations in modern electronics, so researchers have proposed the use of polymers containing conductive fillers. In the present study, waterborne poly(urethane-imide) (WPUI) composites reinforced with conductive carbon nanostructures (CNS) are developed for EMI shielding applications. NCO-terminated imide oligomers are successfully synthesized, so a solvent is not needed to incorporate imide structures into polyurethane. Additionally, a reactive nonionic dispersant is employed to prevent emissions from amine neutralizers. The proposed WPUI, which has high thermal stability and heat resistance, is thus environmentally friendly. The composites are experimentally evaluated through Fourier transform infrared spectroscopy, differential scanning calorimetry, and tensile stress–strain analysis and furthermore subjected to an EMI shielding test. Compared with polyurethane, the WPUI–CNS composite has considerably superior tensile strength and flexibility. Incorporating 5 wt% CNS into WPUI results in an EMI shielding effectiveness of 50 dB and does not negatively affect the WPUI's favorable physical properties, which is not the case for current alternatives. The optimal WPUI composite is found to have excellent performance under high-temperature conditions.

1 | Introduction

The proliferation of electronic devices and wireless communication technology has led to the increased production of electromagnetic waves (EMWs), which can interfere with other electronic devices and potentially pose health risks to living organisms, especially when wave exposure is prolonged. Although traditional metals such as copper, nickel, and aluminum are effective materials for electromagnetic interference (EMI) shielding, their high density, susceptibility to corrosion, complex processing, and limited flexibility restrict their application in modern electronics [1–3]. To address this problem, researchers have begun to focus on polymers and composites, which are lightweight, corrosion-resistant, and cost-effective solutions for EMI shielding [4]. Polymers with a backbone of conjugated double bonds exhibit high electrical conductivity and unique electronic properties. This conductivity arises from the movement of delocalized π-electrons when an electric field is applied. However, the rigid structure of their molecular chains leads to poor processing performance. In contrast, conventional polymers are generally insulating but can become conductive by incorporating fillers, which allows for a more flexible structural design. In the development of effective EMI shielding materials, scholars have utilized conductive fillers such as carbon

nanotubes, graphene, metal nanoparticles, and transition metal carbide [5–8]. These fillers enhance the electrical conductivity of polymers, making them more effective at blocking or absorbing EMWs. In addition to enhancing shielding performance, these composites have great potential to serve multiple functions. They can enhance hydrophobicity to confer water resistance, are flame-retardant, exhibit excellent thermal conductivity, offer transparency, and even possess self-healing capability [9–12]. The development of multifunctional EMI shielding materials is crucial for expanding their application in various industries, including consumer electronics, aerospace, and medical device industries. However, challenges such as material compatibility and integration remain to be addressed. Future research should focus on optimizing material combinations, improving processing techniques, and exploring novel approaches for enhancing the multifunctionality of EMI shielding materials.

Polyurethane (PU) has been regarded as a specialized material because of its block copolymer structure, which contains a distinct soft segment (SS) and hard segment (HS). The SS predominantly influences low-temperature performance and elasticity, whereas the HS controls high-temperature performance and hardness. Therefore, PU can be customized for specific applications by adjusting the ratio of SS to HS or modifying the compositions of these segments [13]. Although PU has the aforementioned advantages, its thermal instability and deformation limit its potential applications, and the PU structure must be modified to overcome these limitations. The literature indicates that embedding heterocyclic structures—such as oxazolidone, triazine, and phosphazene—into PU can enhance its thermal resistance [14–16]. In the present study, the focus was on incorporating imide structures into PU. Polyimide (PI) offers stability at high temperatures, excellent mechanical properties, and chemical resistance. PI is used in various industrial applications to replace traditional materials such as glass, metals, and even steel. However, the high production costs and demanding high-temperature processing requirements of PI limit its widespread use [17, 18]. Incorporating an imide structure into the PU structure can result in the creation of elastic and heat-resistant poly(urethane-imide) (PUI) material. This approach leverages the advantageous properties of both PU and PI, potentially expanding the range of application of PU in demanding environments [19].

Imide structures can be incorporated into PU through various methods, as illustrated in Figure 1. One approach involves dissolving an anhydride in a small quantity of aprotic polar solvent and allowing it to react with isocyanate groups and integrate into the main polymer chain [20]. In another method, an anhydride is modified to form an imide structure with hydroxyl groups at both ends; these hydroxyl groups facilitate the anhydride's reaction with isocyanate groups and its subsequent incorporation into the main chain [21]. These methods typically require the use of an aprotic polar solvent, which poses risks to operators and the environment. Moreover, increasing environmental awareness and stringent regulations, such as the Clean Air Act in the United States and the German TA-Luft, have placed limits on the acceptable level of solvent emissions, necessitating the development of water-based systems [22]. This shift has resulted in the advancement of waterborne poly(urethane-imide) (WPUI). An alternative approach that avoids this problem involves directly reacting an aliphatic isocyanate with an anhydride. In this approach, the aliphatic isocyanate serves both as a reactant and as a solvent [23]. The aforementioned reaction produces an isocyanate-terminated imide oligomer; the need for additional solvents is eliminated, and associated safety and environmental problems are mitigated.

Replacing the solvent with water for dispersing PUI requires the introduction of an ionic system or emulsifier. A crucial step in this process is the ionization of carboxylic acid monomers using neutralizing agents like triethylamine (Figure 1). This step is essential for achieving effective dispersion of PUI resins in water [24]. However, these amine-based monomers often volatilize and release free amines during the WPUI manufacturing process. To ensure that a reaction is environmentally friendly, solvent usage should be reduced, and the content of volatile organic compounds should be minimized. The cationic sulfonate system is a viable solution for manufacturing WPUI; however, it must be dissolved in dispersing water and used as a chain extender [25]. This process can lead to colloidal aggregation caused by temperature drops before dispersion, with such aggregation making

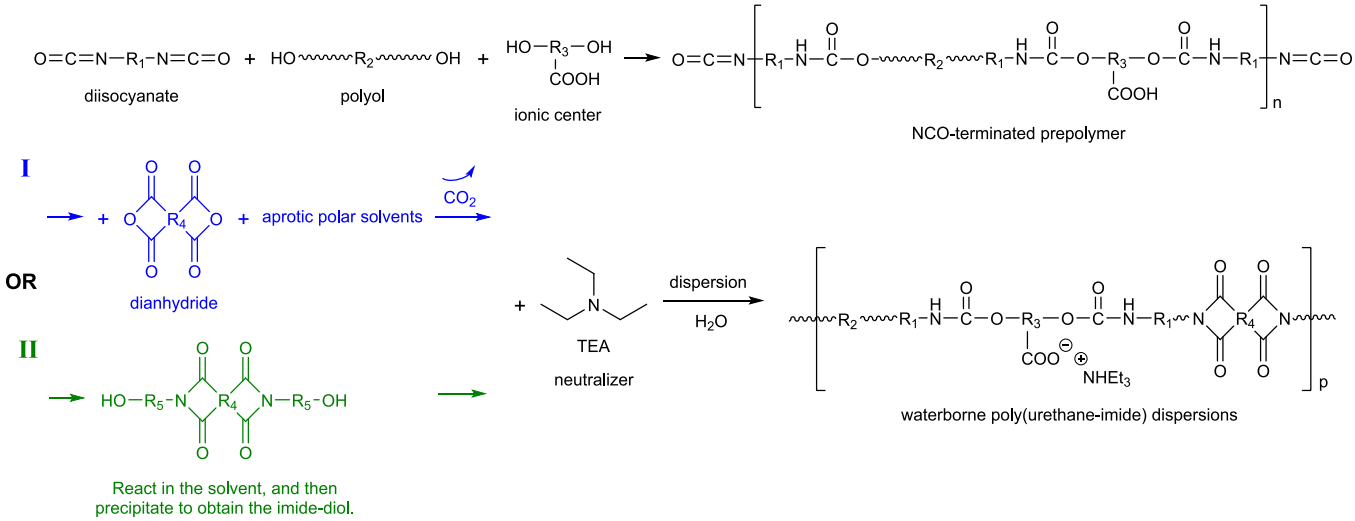

FIGURE 1 | Solutions for manufacturing WPUI. [Color figure can be viewed at wileyonlinelibrary.com]

ionization difficult. Nonionic hydrophilic monomers that can react with isocyanates are a better choice. These monomers contain two primary hydroxyl groups that can be integrated into the backbone of PUI. Moreover, the ethoxylated branch chain of the monomers can disperse PUI in water [26]. When nonionic hydrophilic monomers are used, processing is easy, amines need not be neutralized, and the electrolyte is more stable.

Carbon-based fillers are preferred over metal nanoparticles or nanowires as conductive fillers as they offer advantages in reducing weight, lowering costs, and enhancing stability across various environments. They can have various morphologies and include multiwalled carbon nanotubes (MWCNTs), which have a rod-like structure; graphene nanoplatelets (GNPs), which are thin sheets with a platelet structure; and carbon nanostructures (CNSs), which have a tree-like morphology with branched crosslinked structures [27, 28]. In a previous study, electrically insulating thermoplastic polyurethane (TPU) was shown to have surface resistance greater than $10^{12}\,\Omega$; the addition of 2 wt% CNS considerably reduced this resistance to $10^{4}\,\Omega$, whereas the addition of the same amount of MWCNT or GNP resulted in TPU with a resistance similar to that of the pure TPU. These findings demonstrated the strong ability of CNS to form a conductive network within TPU [29]. Therefore, CNSs enable the creation of composites with a lower percolation threshold than that of MWCNT, which results in less filler being required and helps preserve the mechanical properties of the composite. Incorporating CNS into WPUI materials can thus enable the desired conductivity to be achieved while maintaining mechanical integrity.

The rising demand for eco-friendly and effective EMI shielding materials has led to a focus on the development of multifunctional polymer composites. The objective of this study was to enhance the WPUI manufacturing process to enable the synthesis of solvent-free and amine-free WPUI. To further improve the material's performance, thermal stability was enhanced through the incorporation of imides. Additionally, by incorporating a lower amount of CNS, the conductivity and EMI shielding effectiveness (EMI SE) of WPUI were improved without compromising its mechanical properties. Furthermore, this study systematically evaluated the thermal stability, mechanical properties, and EMI SE of the produced polymers.

2 | Experimental Section

2.1 | Materials

Isophorone diisocyanate (IPDI), which has an equivalent weight of $111.2\,g\,mol^{-1}$, was procured from Covestro (Leverkusen, Germany). Pyromellitic dianhydride (PMDA) and pyromellitic acid (PMA) were supplied by Tokyo Chemical Industry (Osaka, Japan). Prior to use, these powders were dehydrated at 70°C for 24 h. Polycaprolactone (PCL) and poly(tetramethylene ether glycol) (PTMG), both of which have an average molecular weight of $2000\,g\,mol^{-1}$, were supplied by Daicel (Osaka, Japan) and Dairen Chemical Corp. (Taipei, Taiwan), respectively. These polyols were vacuum-dried at 90°C for 24 h at a pressure of 10 Torr and stored in a desiccator until use. Ymer N120 dispersant, which was sourced from Perstorp (Malmö, Sweden), was vacuum-dried at 70°C and 10 Torr for 24 h before use. The chain extender ethylenediamine (EDA) was procured from Thermo Fisher Scientific (Waltham, MA, USA). CNSs (ATHLOS CNS) were acquired from Cabot (Boston, MA, USA). All chemicals were used as received, without further purification.

2.2 | Synthesis of NCO-Terminated Imide Oligomer

An experiment was conducted in which IPDI, PMDA, and PMA were placed in a round-bottom flask equipped with a mechanical stirrer and thermometer. The flask was subjected to condensation reflux, with the temperature gradually increased to 140°C. This process caused the anhydride to dissolve in the isocyanate, forming a clear mixture. The reaction was continued until bubbles had disappeared and the remaining NCO percentage had reached its theoretical limit, resulting in the formation of an NCO-terminated imide oligomer. The preparation and formulation procedures used to obtain the NCO-terminated imide oligomer are detailed in Scheme 1 and Table 1, respectively. The

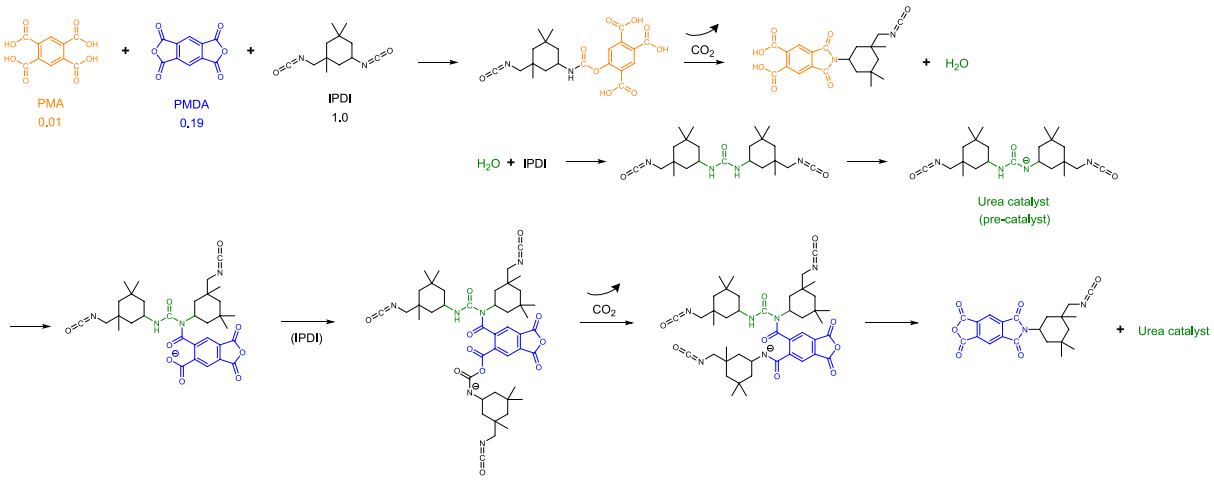

SCHEME 1 | Preparation of an NCO-terminated imide oligomer and the oligomer's reaction mechanism. [Color figure can be viewed at wileyonlinelibrary.com]

formulation code O-15 indicates that "O" stands for oligomer, while "15" specifies the weight percentage of PMDA in the overall oligomer, which has a constant IPDI content. Two different formulations were created to evaluate the effects of varying PMDA levels. The reaction between the isocyanate and carboxylic acid produced a water molecule by-product, which subsequently formed urea. This process increased the rate of reaction of the oligomer [30].

2.3 | Preparation of Water-Based Poly(Urethane-Imide) Dispersion

Vacuum-dried polyol and dispersant were placed in a four-port reaction tank equipped with a stirrer, a thermocouple, and a nitrogen inlet hose. The mixture was stirred until it had become homogeneous. The temperature was then maintained at 85°C, and a heat-softened oligomer was introduced to trigger a reaction, which was continued until the NCO percentage had reached the theoretical equivalent value. Subsequently, the temperature was reduced by 40°C, and EDA and deionized water were introduced for chain extension and dispersion. After 1 h, the mixture was transferred to a homogenizer for high-speed dispersion. This process resulted in the formation of WPUI with 30 wt% solid content. The formulation and preparation procedures used to obtain the WPUI are detailed in Table 2 and Scheme 2, respectively. The experimental design includes several formulations to evaluate the effects of imide functionality, HS content, dispersant level, and polyol type on WPUI film properties. WPU-20, a baseline waterborne PU, contains 20 wt% HS. WPUI-20 also has 20 wt% HS but introduces imide groups with O-15 for comparison with WPU-20,

TABLE 1 | Formulation of an NCO-terminated imide oligomer.

Code	IPDI (En[a]; g)	PMDA (En; g)	PMA (En; g)	Theoretical remaining NCO% (%)	Equivalent weight (*E*)	PMDA content (wt%)
O-15	1.0; 111.2	0.19; 20.7	0.01; 1.3	24.6	171.4	15
O-20	1.0; 111.2	0.27; 29.5	0.03; 3.8	18.5	227.1	20

[a]Mole equivalent.

TABLE 2 | Formulation of WPUI.

Code	Oligomer (En; g)	PCL (En; g)	PTMG (En; g)	Ymer N120 (En; g)	EDA (En; g)	HS (%)
WPU-20	IPDI (0.52; 57.3)	0.1; 100	—	0.10; 51.0	0.30; 9.1	20
WPUI-10	O-15 (0.31; 53.0)	0.1; 100	—	0.10: 51.0	0.10; 3.0	10
WPUI-20	O-15 (0.44; 75.1)	0.1; 100	—	0.10; 51.0	0.23; 6.8	20
WPUI-30	O-15 (0.60; 103.5)	0.1; 100	—	0.10; 51.0	0.39; 11.6	30
WPUI-O-20	O-20 (0.40; 90.6)	0.1; 100	—	0.10; 51.0	0.19; 5.6	20
WPUI-Ymer15	O-15 (0.53; 92.5)	0.1; 100	—	0.15; 76.5	0.26; 7.9	20
WPUI-PTMG	O-15 (0.44; 75.1)	—	0.1; 100	0.10; 51.0	0.23; 6.8	20

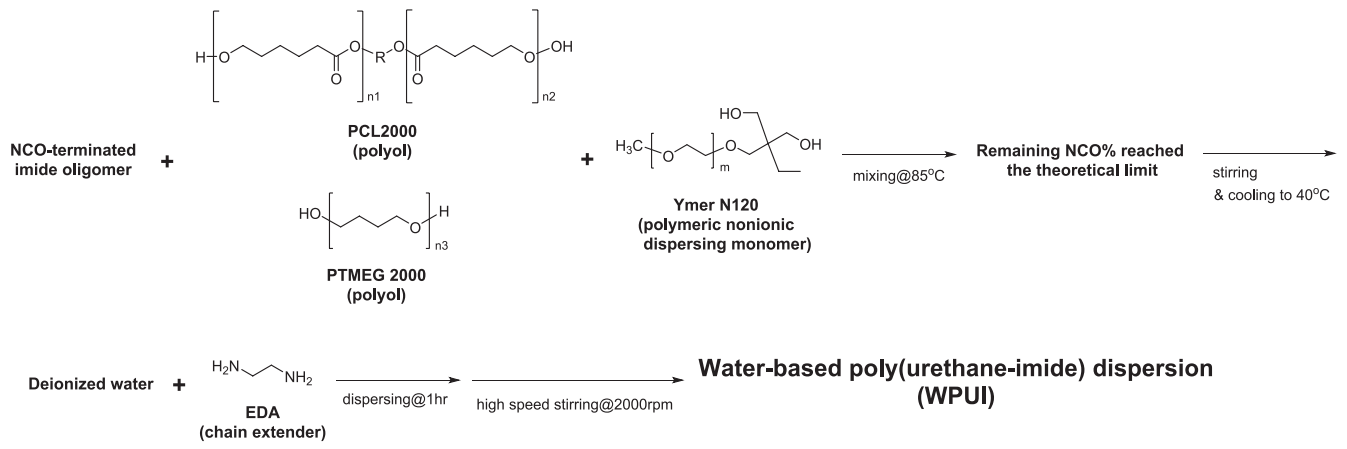

SCHEME 2 | Preparation of WPUI.

which lacks imide functionality. Variations like WPUI-10 and WPUI-30 adjust the HS content relative to WPUI-20 to assess its impact, while WPUI-O-20 uses O-20 instead of O-15 to explore a higher imide content. WPUI-Ymer15 increases the dispersant concentration from 0.10 to 0.15, and WPUI-PTMG replaces the polyol PCL with PTMEG to examine how polyol type influences film properties.

2.4 | Preparation of WPUI Films and EMI-Shielding WPUI Films

CNS powder with amounts of 2, 5, and 10 wt% was incorporated into the preprepared WPUI-20 dispersions. Each mixture was homogenized at 2000 rpm. Next, a high-pressure homogenizer (Genizer; NanoGenizer series) was used to thoroughly homogenize the samples; this process involved employing high pressure to propel the liquid and powder within a sample through a narrow-gapped valve, which induced considerable shear, a pressure drop, and cavitation. This approach has been shown to effectively promote filler dispersion and enhance the formation of conductive networks in polymer matrices, as supported by the findings of Yan Li et al. [31] Their study demonstrated that high-pressure homogenization can achieve uniform dispersion of conductive fillers, thereby improving the performance of composite materials without the need for complex structural design or prefabrication of the fillers.

The dispersions obtained were named WPUI-CNS-2, WPUI-CNS-5, and WPUI-CNS-10. For the purpose of comparison, an additional dispersion of WPUI-20 containing 2 wt% carbon black (CB; Cabot VULCAN XC72) was prepared (designated WPUI-CB-2) by following the same process. All samples were prepared following the same procedure. The required quantity of each dispersion was poured into polytetrafluoroethylene molds and dried in a hot air circulation oven at 40°C. Once the films were dry, they were baked at 70°C for 1 h to ensure that their moisture content was eliminated, resulting in a final sample thickness of 1 mm.

2.5 | Measurements

Fourier transform infrared (FTIR) spectra of the samples were obtained using a JASCO FT/IR-4600 spectrometer in the attenuated total reflection mode; the spectra were scanned 32 times at a spectral resolution of 4 cm^{-1}. The size distribution of the particles in dispersions was assessed using a NanoBrook 90Plus PALS device that utilizes dynamic light scattering. Samples were diluted with deionized water at a 1:2000 ratio and maintained at 23°C during testing. Scanning electron microscopy (SEM) analysis was conducted using a Hitachi Regulus 8100 field-emission scanning electron microscope, with cross-sectional images of the film samples being obtained. Samples were cooled in liquid nitrogen for 10 min to make them brittle and were then fractured to expose their cross section.

Tensile stress–strain data for tension-molded sheets obtained from dumbbell-shaped samples (ASTM D-638, type V) were acquired using a Cometech QC-508M2F testing machine at an extension rate of 100 mm min^{-1}, a temperature of 23°C, and a gauge length of 20 mm.

Differential scanning calorimetry (DSC) analysis was performed using a Hitachi model 7000X DSC device. Each sample (5 mg) was sealed in an aluminum pan and scanned against a blank aluminum pan reference at a heating rate of 20°C min^{-1} over a temperature range of −80°C to 200°C under a nitrogen atmosphere. Thermogravimetric analysis (TGA) was conducted using a Hitachi STA7200 thermogravimeter at a heating rate of 10°C min^{-1} over a temperature range of 23°C to 700°C under a nitrogen atmosphere. Dynamic mechanical analysis (DMA) of rectangular samples (20 mm × 5 mm × 0.5 mm) was conducted using a TechMax DMS 6100 thermal analyzer at a heating rate of 10°C min^{-1} over a temperature range of −80°C to 150°C under a forced vibration frequency of 1 Hz.

An EMI shielding test was conducted in accordance with the ASTM D4935-18 standard by using a Keysight E5071C ENA vector network analyzer (VNA). Samples with a thickness of 1 mm were cut such that they could cover a 20 mm × 10 mm current path. The test was performed using the coaxial transmission line method in the X-band frequency range (8.2–12.2 GHz). Surface resistivity testing was conducted using a Mitsubishi Chemical MCP-T600 four-point probe model under a stable DC voltage to measure the surface resistance of the samples; the probe was configured to move in a straight line, and the probe spacing was 1 mm.

2.6 | Methods for Characterizing EMI Shielding

EMI shielding involves the use of materials that can reflect and absorb EMWs to protect sensitive components from interference. The effectiveness of a material in shielding against EMI, known as EMI SE, is measured in decibels (dB) and indicates the ratio of incoming energy to the energy that remains. According to Schelkunoff's theory, EMI SE consists of three main components: reflection loss (SE_R), absorption loss (SE_A), and multiple reflection loss (SE_M). These components are combined as follows: [32]

$$SE_T = SE_R + SE_A + SE_M \quad (1)$$

Reflection loss occurs due to impedance mismatches between free space (such as air) and the shielding material. This mismatch leads to interactions between charged particles and the electromagnetic field. Absorption loss primarily arises from the interactions between EMWs and movable charge carriers, as well as electric and magnetic dipoles within the material. Multiple reflection loss happens when EMWs entering the shield are repeatedly reflected and transmitted within the material. Collectively, these losses contribute to the overall effectiveness of the material in shielding against EMI.

EMI SE can be measured by monitoring changes in EMW power or phase as it passes through a shield using a network analyzer (NA). VNAs are preferred due to their capability to measure complex signals, such as permittivity and permeability. The transmission line method is the most commonly used approach because of

its wide frequency range and efficiency. This method includes the waveguide, which has a simple setup but requires multiple waveguides to cover a broad frequency range, and the coaxial transmission line, which is ideal for far-field measurements. Using a VNA, scattering parameters (S_{11}, S_{22}, S_{12}, S_{21}) are calculated to evaluate the EMI SE, as illustrated in Figure 2. These S parameters represent the reflection and transmission coefficients: S_{11} and S_{22} indicate forward and reverse reflections, while S_{12} and S_{21} represent forward and backward transmissions, respectively. According to shielding theory, the incident EMW is divided into power coefficients of reflection (R), absorption (A), and transmission (T), following the relation $R+A+T=1$ [33, 34].

$$T = |S_{12}|^2 = |S_{21}|^2 \tag{2}$$

$$R = |S_{11}|^2 = |S_{22}|^2 \tag{3}$$

$$A = 1 - R - T \tag{4}$$

Additionally, the SE_T, SE_A, and SE_R can be defined as follows, considering that SE_M is typically disregarded when the SE_T exceeds 15 dB [35].

$$SE_T = 10\log\left(\frac{1}{|S_{12}|^2}\right) = 10\log\left(\frac{1}{|S_{21}|^2}\right) = 10\log\left(\frac{1}{T}\right) \tag{5}$$

$$SE_R = 10\log\left(\frac{1}{|S_{11}|^2}\right) = 10\log\left(\frac{1}{|S_{22}|^2}\right) = 10\log\left(\frac{1}{1-R}\right) \tag{6}$$

$$SE_A = 10\log\left(\frac{1-|S_{11}|^2}{|S_{12}|^2}\right) = 10\log\left(\frac{1-|S_{22}|^2}{|S_{21}|^2}\right) = 10\log\left(\frac{1-R}{T}\right) \tag{7}$$

The absorption attenuation of EMI shields is characterized by the introduction of the effective absorption fraction (A_{eff}) [36].

$$A_{eff} = \frac{1-R-T}{1-R} \times 100\,\% \tag{8}$$

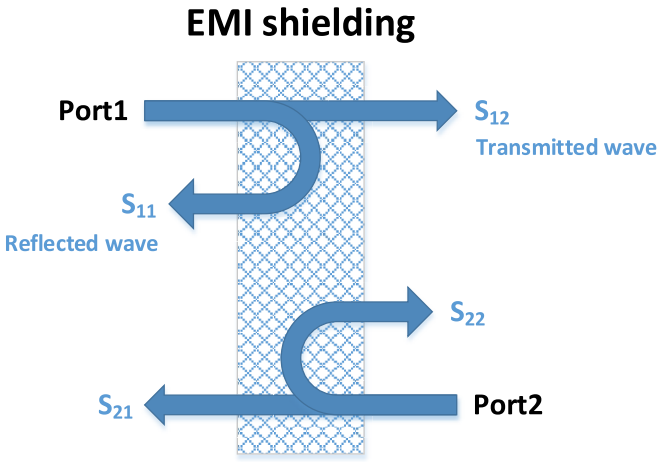

FIGURE 2 | Complex scattering parameters of EMI shielding materials using a two-port VNA. [Color figure can be viewed at wileyonlinelibrary.com]

3 | Results and Discussion

3.1 | FTIR Analysis

Figure 3 displays the FTIR spectra of IPDI and PMDA. The FTIR spectrum of IPDI contained an absorption peak at 2247 cm^{-1}, indicating the presence of NCO functional groups. Additionally, the spectrum of PMDA contained two absorption peaks related to carbonyl groups (C=O): at 1805 cm^{-1} for symmetric stretching and at 1762 cm^{-1} for asymmetric stretching. The NCO-terminated oligomer (O-20) underwent imidization, forming imide groups, which led to a reduction in the NCO peak intensity in the FTIR spectrum of the oligomer. The reduction rate was determined to be 50.7% (calculated as the area under the tangent line from 2500 to 2115 cm^{-1}), consistent

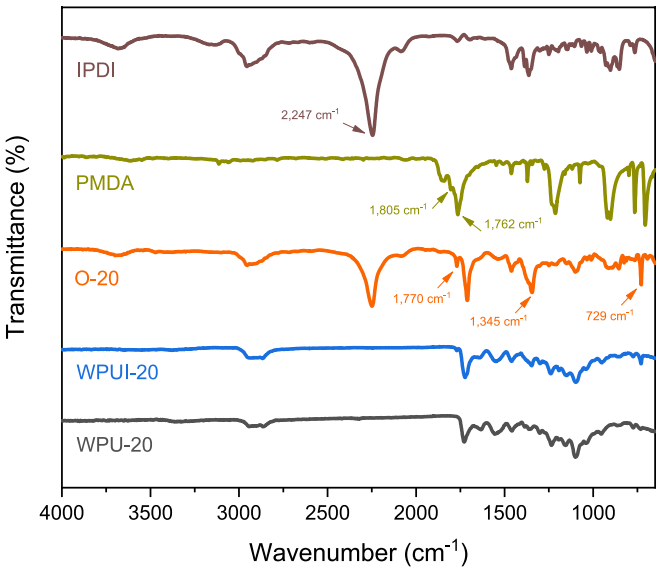

FIGURE 3 | FTIR spectra of the raw materials and the WPUI film. [Color figure can be viewed at wileyonlinelibrary.com]

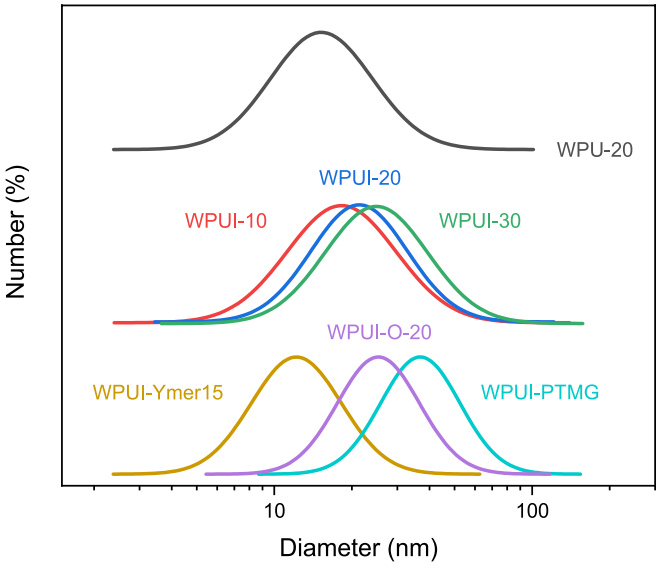

FIGURE 4 | D_{50} particle size distribution curve of WPUI dispersions. [Color figure can be viewed at wileyonlinelibrary.com]

TABLE 3 | Particle sizes and mechanical properties of WPUI materials.

Code	Dispersant (Ymer N120) (wt%)	D_{50} (nm)	100% modulus (MPa)	Tensile strength at break (MPa)	Elongation at break (MPa)	Toughness (GJ m^{-3})
WPU-20	23.5	14.9	2.5	5.2	317	1.2
WPUI-10	24.6	17.9	0.4	4.9	728	1.0
WPUI-20	21.9	21.5	2.8	17.0	489	3.0
WPUI-30	19.2	25.3	5.9	19.9	272	2.3
WPUI-O-20	20.6	25.6	3.7	25.1	416	3.4
WPUI-Ymer15	27.6	12.4	1.6	8.9	644	2.4
WPUI-PTMG	21.9	37.1	1.9	4.2	415	1.1

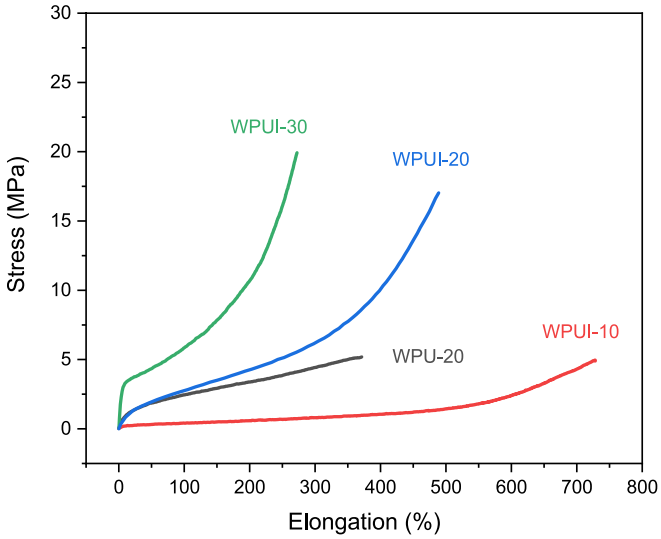

FIGURE 5 | Stress–strain curve of WPUI films with varying HS contents. [Color figure can be viewed at wileyonlinelibrary.com]

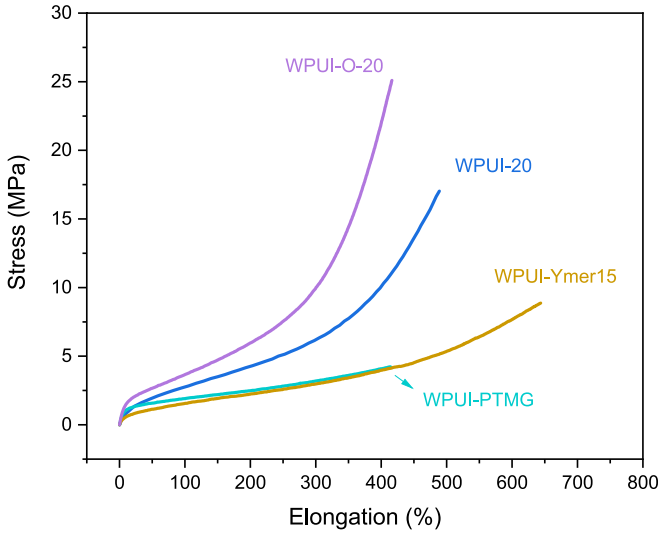

FIGURE 6 | Stress–strain curve of WPUI films with different SS and HS structures. [Color figure can be viewed at wileyonlinelibrary.com]

with the observed difference in the NCO percentage (IPDI: NCO% = 37.8%; oligomer: NCO% = 18.5%). Furthermore, C═O stretching signals at 1805 and 1762 cm^{-1} were absent, confirming that an imide structure had been created in the O-20 oligomer [37]. This result was supported by the signals corresponding to a cyclic five-membered imide ring, namely, the signals associated with in-phase C═O vibration absorption, C–N–C stretching, and out-of-phase bending at 1770, 1345, and 729 cm^{-1} [38]. When a film was formed, the NCO absorption peaks (2247 cm^{-1}) in the spectra of WPUI-20 and WPU-20 disappeared, indicating a complete reaction.

3.2 | Size Distribution Analysis

The size of particles in WPUI dispersions is influenced by several key factors. Decreasing the HS content and increasing the weight ratio of the dispersant Ymer N120 are effective strategies for reducing the D_{50} particle size in WPUI dispersions (please refer to Figure 4 and Table 3). For example, reducing the HS content from WPUI-30 to WPUI-10 led to a 29% decrease in D_{50}. Additionally, increasing the dispersant content from 0.1 in WPUI-20 to 0.15 in WPUI-Ymer15 resulted in a 42% reduction in D_{50}. It is also essential to consider factors that may lead to an increase in particle size. Substituting the polyol in a polyester system (WPUI-20) with a polyether system (WPUI-PTMEG) tends to increase the particle size because of the high hydrophobicity of polyether polyol [39]. Moreover, incorporating imide groups into the structure of the HS or increasing their concentration under a fixed HS ratio results in larger particles. This phenomenon is attributable to increased stronger intermolecular interactions, leading to polymer chain aggregation and dispersion with larger particles [40]. To ensure that this study's WPUI dispersions were stable, they were centrifuged at 3000 rpm for 15 min. The absence of precipitation indicated the feasibility of using Ymer N120 as a dispersant for maintaining the dispersions' stability, highlighting its suitability for practical applications.

3.3 | Mechanical Properties

The stress–strain curves shown in Figures 5 and 6 indicate how adjustments to the structural design of WPUI affect its physical properties. The relevant physical values are listed in Table 3. Figure 5 indicates that as the HS content was increased (from

WPUI-10 to WPUI-30), the 100% modulus and tensile strength of the prepared WPUI samples tended to rise, whereas their elongation decreased. These results suggest that the HS content of WPUI can strongly influence its rigidity. However, the PUI systems with a high HS content did not become brittle, thus sacrificing their toughness. Finding a balance between rigidity and flexibility is crucial. Studies have shown that PUI films with elastic-like or plastic-like characteristics can be produced by adjusting the structure or content of the SS and HS [19]. In the present research, WPUI-20 had an optimal balance of these characteristics. Apart from HS content, an increase in the imide concentration from 5.0 wt% in WPUI-20 to 7.5 wt% in WPUI-O-20 also improved the 100% modulus and tensile strength, as shown in Table 3. This enhancement was attributable to the intermolecular interaction of charge transfer complexes, highlighting the role of molecular interactions in dictating the mechanical behavior of WPUI [23]. Specific structural designs may reduce the mechanical strength. Figure 6 illustrates that the polyester-based SS structure (WPUI-20) led to a higher 100% modulus and greater toughness than did the ether-based structure (WPUI-PTMG) due to the stronger hydrogen bonds provided by esters relative to ethers [41]. Additionally, increasing the dispersant content from 0.1 in WPUI-20 to 0.15 in WPUI-Ymer15 led to a decrease in the modulus and increased the elongation due to the ether groups in the dispersant structure. Based on the discussion above, this study will use WPUI-20 as the foundational material for adding CNS.

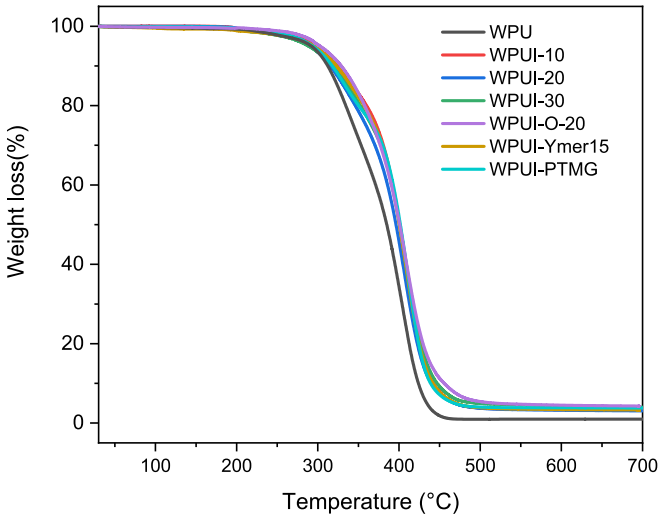

FIGURE 7 | Thermogravimetric loss curves of the fabricated WPUI films. [Color figure can be viewed at wileyonlinelibrary.com]

3.4 | Results of TGA

According to the literature, PUI typically degrades in three distinct stages [42]. The initial stage, which occurs from 280°C to 360°C, involves degradation of the HS, primarily through the cleavage of urethane bonds. The second stage occurs between 360°C and 440°C and is characterized by SS degradation. Finally, the third stage, which occurs at temperatures higher than 500°C, entails degradation of the imide structures within the polymer backbone. Figure 7 and Table 4 present the TGA results obtained for the WPUI films. Incorporation of imide groups into the structure of WPU-20 enhanced the $T_{d5\%}$ (5% weight loss temperature) value within the temperature range corresponding to HS degradation in the initial stage. This effect was particularly prominent for WPUI-O-20, which had the highest $T_{d5\%}$ value, attributable to the strong hydrogen bond interactions within the HS [43]. However, as the HS content in the WPUI formulation increased from WPUI-10 to WPUI-30, a decrease in the $T_{d5\%}$ value was observed. This phenomenon can be attributed to the protective effect of the SS present in WPUI-10. Thus, as the HS content increases, the initial degradation temperature decreases. Another reason for the improved thermal stability when reducing the HS content or increasing the SS content is that the degradation of long-chain SS requires a higher thermal energy [44, 45]. Moreover, regarding the thermogravimetric region corresponding to SS loss in the second stage, formulations with higher proportions of Ymer N120 (WPUI-Ymer15) or employing polyether-based polyol (WPUI-PTMG) had lower T_{dmax} (maximum weight loss temperature) values than did the polyester-based WPUI-20. This phenomenon was caused by weak hydrogen bond interactions [46]. In the third stage of pyrolysis, the

TABLE 4 | TGA weight loss and DSC phase transition temperature of the fabricated WPUI films.

Code	5 wt% degradation loss ($T_{d5\%}$; °C)	Maximum degradation loss (T_{max}; °C)	Ash content (%)	T_g (°C)	T_{m1}(SS) (°C)	T_{m2}(SS) (°C)	ΔH_m(SS) (J mg^{-1})
WPU-20	292.2	392.3	1.0	−62.7	28.8	39.2	0.13, 0.53
WPUI-10	299.0	405.2	3.3	−58.7	27.2	35.6	9.9
WPUI-20	290.5	407.7	3.1	−57.6	29.6	40.3	0.6, 0.1
WPUI-30	288.0	408.2	2.2	−55.1	—	—	—
WPUI-O-20	302.8	409.1	4.2	−50.7	—	—	—
WPUI-Ymer15	299.8	402.1	3.1	−58.3	30.1	—	0.4
WPUI-PTMG	291.1	395.4	3.1	−61.8	24.6	—	14.6
Ymer N120	—	—	—	—	22.4	—	24.5
PTMG	—	—	—	—	25.9	—	48.7
PCL	—	—	—	—	—	44.6	45.7

concentration was too low to observe significant thermal degradation of the imide structure, even in WPUI-O-20, which had the highest imide content at 7.5 wt%. Ultimately, compared with the WPU film, all WPUI films had a higher ash content, indicative of superior thermal stability. These findings emphasize the importance of modifying the structure of WPUI films to increase intermolecular forces and enhance the films' thermal stability.

3.5 | Results of DSC Analysis

The distribution of the SS crystal was investigated through DSC analysis of the polyol. As shown in Figure 8 and Table 4, Ymer N120 and PTMG had distinct crystal melting temperatures [denoted T_{m1}(SS)], which were close to the ambient temperature. By contrast, PCL had a T_{m2}(SS) value of approximately 45°C. The aforementioned SS crystallization behavior can strongly affect the thermal and mechanical properties of WPUI [19]. Figure 9 indicates that integration of imide structures into the WPU-20 matrix enhanced HS interactions, leading to a higher enthalpy of fusion [ΔH_m(SS)] in certain regions of the Ymer N120 phase (i.e., WPUI-20). This also led to reduced PCL crystallinity in the SS region and an increase in the glass transition temperature (T_g) [47]. This effect intensified with increasing imide concentration, further suppressing crystallinity and raising the T_g, from −62.7°C in WPU-20 to −50.7°C in WPUI-O-20. Moreover, increasing the HS content in the WPUI formulation (from WPUI-10 to WPUI-30) leads to the suppression of SS crystallization, with this crystallization completely suppressed in WPUI-30 [48]. Figure 10 indicates that as the content of the ether group was increased, the WPUI became more flexible, resulting in a decrease in T_g, with WPUI-Ymer15 and WPUI-PTMG showing lower T_g values than WPUI-20. Furthermore, the ether-type WPUI-PTMG exhibited more pronounced SS crystallization than the ester-type WPUI-20 due to enhanced microphase separation [49]. In cases where the SS melting temperature was close to the room temperature, and the enthalpy of fusion [ΔH_m(SS)] was substantial, as was the case for WPUI-PTMG and WPUI-10, the film tended to be opaque. The results thus indicate that disrupting SS crystallization by increasing the HS content and adjusting the T_g through SS and HS design is an effective method of controlling a film's transparency and thermal stability.

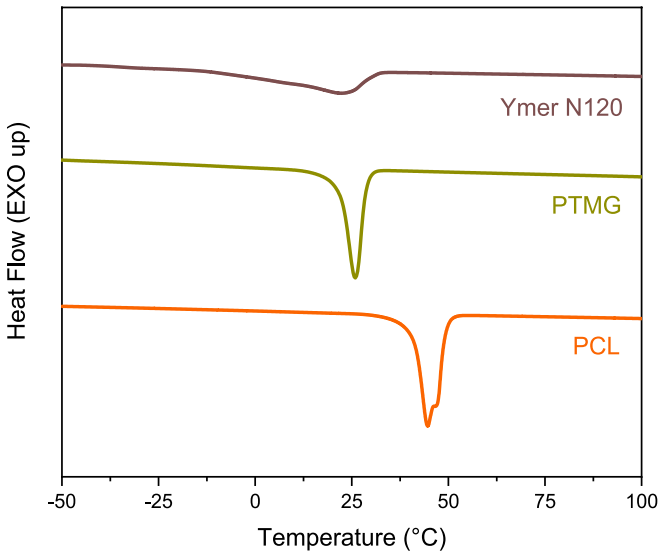

FIGURE 8 | DSC traces for different polyols and dispersants. [Color figure can be viewed at wileyonlinelibrary.com]

3.6 | Results of DMA

The graphs displayed in Figures 11 and 12 illustrate the typical dynamic mechanical properties of the segmented WPUI materials, which were examined through DMA. The curves of tanδ versus temperature for the WPUI copolymer contained two damping peaks: a lower-temperature peak corresponding to the glass transition temperature of the SS [T_g(SS)] and a higher-temperature peak corresponding to the glass transition temperature of the HS [T_g(HS)]. The transition temperature and storage modulus

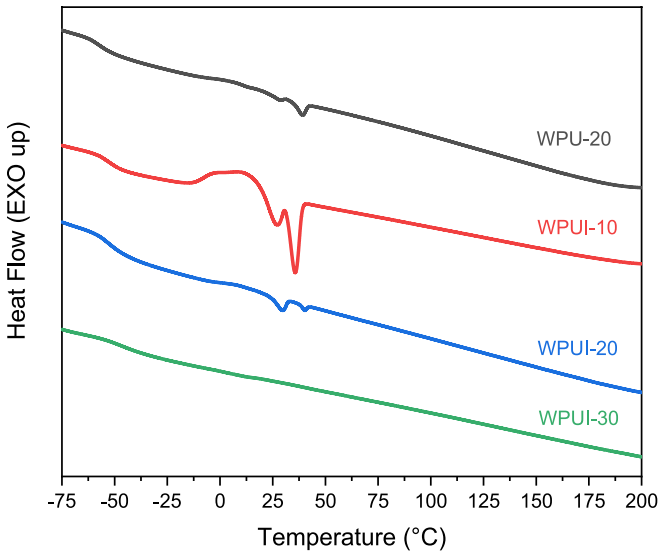

FIGURE 9 | DSC traces for WPUI films with varying HS contents. [Color figure can be viewed at wileyonlinelibrary.com]

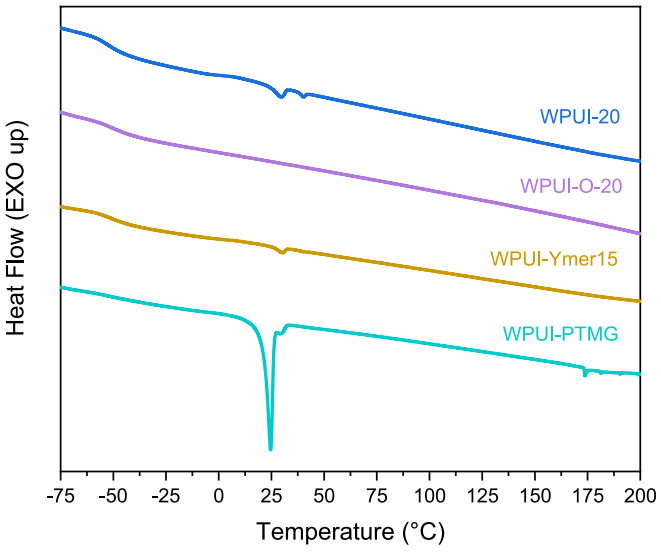

FIGURE 10 | DSC traces for WPUI films with varying SS structures and imide contents. [Color figure can be viewed at wileyonlinelibrary.com]

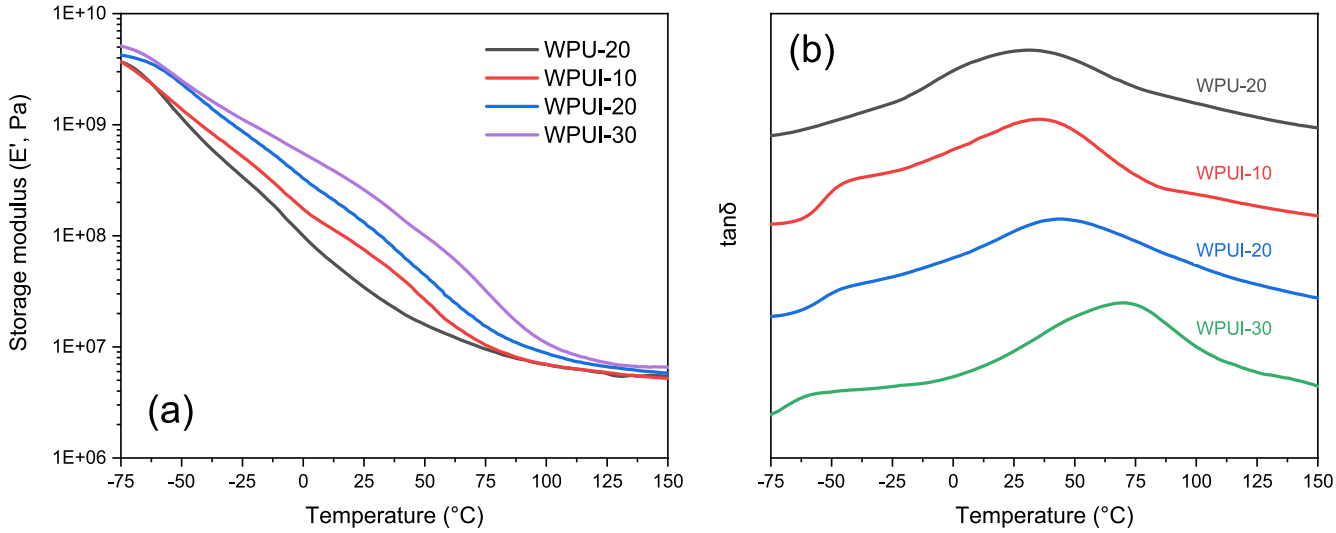

FIGURE 11 | Curves of (a) storage modulus and (b) tanδ versus temperature for WPUI films with varying HS contents. [Color figure can be viewed at wileyonlinelibrary.com]

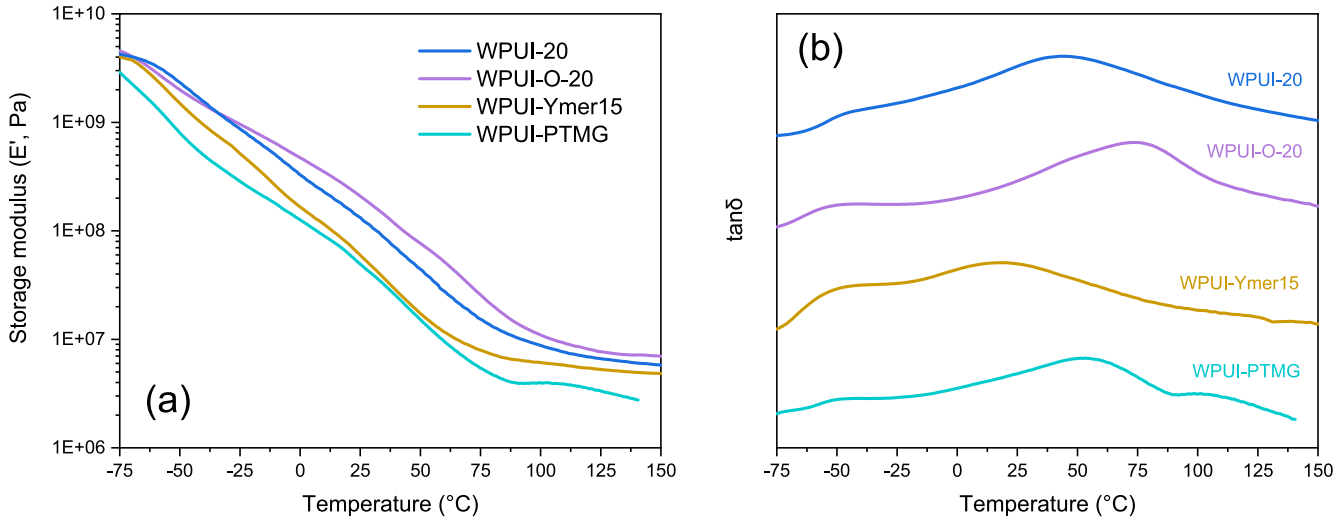

FIGURE 12 | Curves of (a) storage modulus and (b) tanδ versus temperature for WPUI films with varying SS structures and imide contents. [Color figure can be viewed at wileyonlinelibrary.com]

TABLE 5 | DMA transition temperature and storage modulus of the fabricated WPUI films.

Code	T_g (SS)[a] (°C)	T_g (HS) (°C)	E' (100°C) (1E+6 Pa)
WPU-20	—	31.1	7.0
WPUI-10	−41.2	35.3	7.0
WPUI-20	−44.5	44.2	8.7
WPUI-30	−56.4	70.5	10.9
WPUI-O-20	−50.2	75.3	10.9
WPUI-Ymer15	−46.7	17.8	6.1
WPUI-PTMG	−51.4	52.6	4.0

[a]The T_g peak in this presentation is consistently displayed as a shoulder.

results are listed in Table 5. Figure 11 suggests that incorporating imide groups into the WPU-20 main chain induced microphase separation, resulting in two T_g values. When either the imide concentration (WPUI-O-20) or the HS content was higher (from WPUI-10 to WPUI-30), the temperature difference between T_g(SS) and T_g(HS) was greater, indicating a stronger degree of microphase separation [23]. Greater microphase separation is beneficial for thermal stability and mechanical performance, as reflected by the higher storage modulus (E') at 100°C; for example, as shown in Table 5, the E'(100°C) value for WPUI-30 and WPUI-O-20 is approximately 1.6 times higher than that of WPU-20 [50]. Figure 12 suggests that using a higher concentration of the dispersant Ymer N120 (material WPUI-Ymer15) resulted in lower T_g(HS) and E'(100°C) compared to WPUI-20, indicating reduced thermal resistance. Moreover, utilizing polyether-based PTMG as the polyol led to more favorable microphase separation due to the flexible nature of polyethers; however, this resulted in a lower E'(100°C) because of the weaker intermolecular forces of polyethers compared to those of polyesters [49]. This effect was evident in the comparison of WPUI-PTMG with WPUI-20. The aforementioned results highlight the importance of microphase morphology, which affects the T_g behavior of SS and HS and the thermomechanical strength properties of WPUI films.

3.7 | EMI Shielding Analysis

In the design of a composite made from a WPUI dispersion and CNS powder, considering the trade-off between modulus enhancement and toughness reduction is essential. Table 6 and Figure 13a indicate that the plots of Young's modulus and toughness versus CNS content intersected at a CNS content of 2.4 wt%. However, the figure suggests that the optimal balance between modulus and toughness can be achieved with CNS additions between 4 and 6 wt%.

The electrical conductivity of WPUI composites depends on the spatial distribution of conductive fillers and the formation of internal conductive pathways. As shown in Table 6, the EMI SE of WPUI improved significantly with the addition of CNS. A comparison between equal amounts of CB and CNS in WPUI revealed that using CNS resulted in a 9-fold increase in EMI SE. This substantial improvement is attributed to the high electrical conductivity of CNS, which are cross-linked, branched carbon nanotubes. Even at low concentrations, CNS formed effective conductive networks. SEM images in Figure 14 further indicate that CNSs were uniformly distributed within the WPUI-CNS-5 film and formed a fine, interwoven structure. This overlapping network created enhanced pathways for electron mobility, effectively lowering the material's resistance. Additionally, CNS established more efficient interconnections compared to CB, leading to the development of superior charge conduction paths within the insulating polymer matrix [29]. The relationship between EMI SE and

TABLE 6 | Physical and mechanical properties of WPUI with varying CNS contents.

Code	Young's modulus (MPa)	Toughness (GJ m^{-3})	EMI shielding effectiveness (EMI SE; dB)	Surface resistance (ohm $sq.^{-1}$)
WPUI-20	12.3	3.0	0.6	> 1E+09
WPUI-CNS-2	41.1	1.5	33.1	20.0
WPUI-CNS-5	162.8	1.7	50.7	1.8
WPUI-CNS-10	110.9	1.1	57.4	0.9
WPUI-CB-2	—	—	3.6	> 1E+03

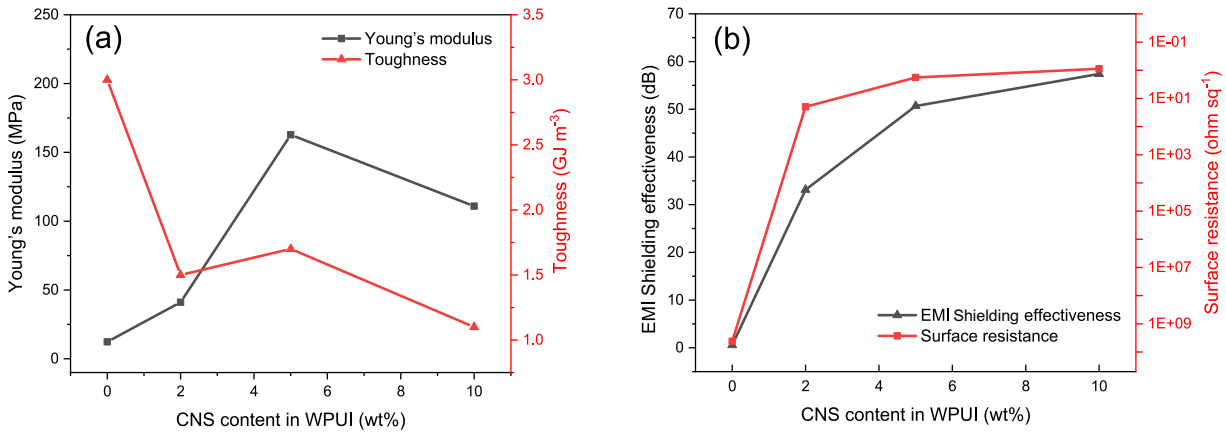

FIGURE 13 | (a) Intersection of plots of toughness and Young's modulus versus CNS content for WPUI; and (b) surface resistivity of WPUI films with varying CNS contents. [Color figure can be viewed at wileyonlinelibrary.com]

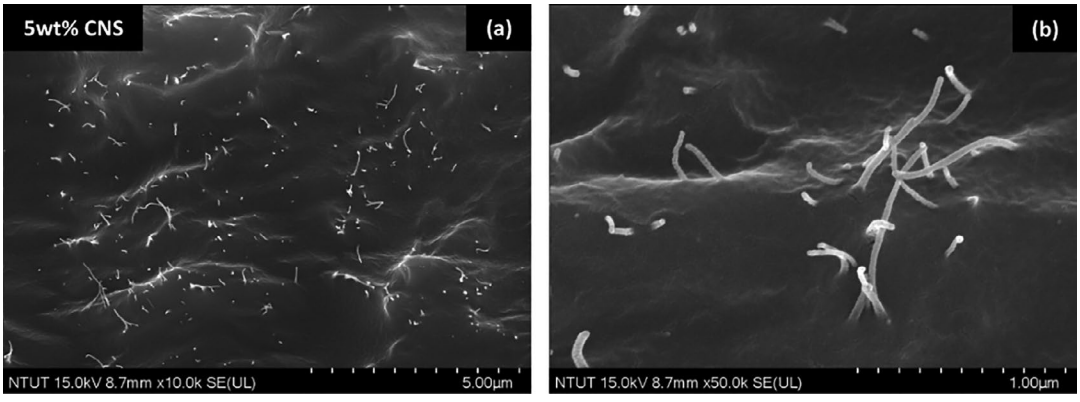

FIGURE 14 | SEM images of WPUI-CNS-5 at (a) 10,000× and (b) 50,000× magnification.

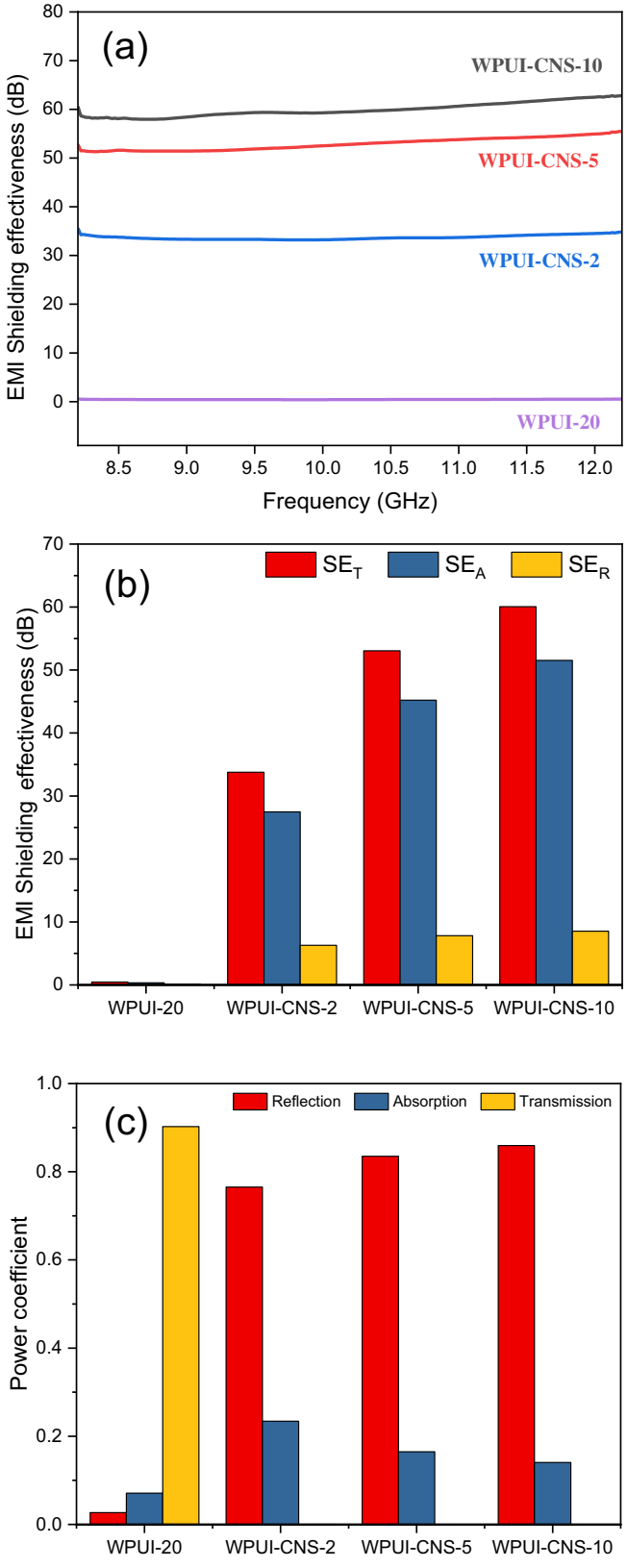

FIGURE 15 | (a) EMI SE in the X-band frequency range; (b) SE_T, SE_A, and SE_R analyses of WPUI films with varying CNS contents; and (c) power coefficients of *T*, *R*, and *A* of WPUI films. [Color figure can be viewed at wileyonlinelibrary.com]

surface resistance is depicted in Figure 13b, showing that lower surface resistance corresponds to higher SE. However, the reduction in surface resistance due to CNS content has a limit; beyond approximately 5 wt% CNS content, the decrease in surface resistance and the corresponding improvement in SE began to plateau. Therefore, considering both physical properties and electromagnetic SE, WPUI-CNS-5 may be the optimal formulation.

The SE_T value is positively correlated with the sample thickness, which is why this study fixed the thickness at 1 mm for the EMI SE analysis. As shown in Figure 15a, the SE_T increases significantly with the addition of CNS in the WPUI film, reaching 50 dB at a content of 10 wt%, which corresponds to an A_{eff} of 99.999% SE, thus meeting the commercial product requirement of 30 dB. To gain insight into the underlying mechanisms, Figure 15b further illustrates the SE_T, SE_R, and SE_A values, showing that the SE_A values were notably higher than the SE_R values across all samples, suggesting that absorption was the primary mechanism for EMW attenuation within the nanocomposite samples. However, these results alone do not fully clarify the EMI shielding mechanism of the material system, so a further analysis of the power coefficients *T*, *R*, and *A*, as depicted in Figure 15c, was conducted [36].

The analysis of power coefficients reveals that the *R* values of all samples were significantly higher than the *A* values, indicating that most EMWs were reflected before penetrating the samples. Although the *R* value increased with the addition of CNS due to enhanced conductivity, the increase was not substantial, likely because the percolation threshold—the minimum concentration of filler at which an insulating material transitions to a conductive state—had already been reached [35]. Beyond this point, further addition of a conductive filler yields diminishing returns in reflection efficiency, as the conductive network within the composite has already been established. However, high reflection can lead to significant secondary EMI pollution. To address this, incorporating magnetic fillers into the composite design can help reduce reflection loss and mitigate secondary radiation, thereby optimizing the overall EMI shielding performance [51]. While WPUI-CNS-5 demonstrates superior EMI shielding performance, further investigation into the long-term stability of the conductive networks, as well as the effect of different types of magnetic fillers, could provide valuable insights into further optimization of the composite for industrial applications.

4 | Conclusions

This study successfully synthesized NCO-terminated imide oligomers, eliminating the need to use a solvent for the incorporation of imide structures into PU. In addition, a reactive nonionic dispersant was selected to mitigate concerns regarding volatile organic compound emissions from amine neutralizers. The final result was an environmentally friendly WPUI dispersion with high emulsion stability, flexibility, and heat resistance. The size of particles in the WPUI dispersion can be controlled by adjusting the quantity of nonionic dispersant used, with higher concentrations leading to smaller particles and higher dispersion stability. However, the presence of ether groups in the dispersant may reduce the tensile strength of WPUI films. Strategies for enhancing a WPUI film's strength include increasing the content of HS, increasing the imide concentration, or selecting SS structures with ester groups, which offer stronger

hydrogen bonding than ether groups do. Intermolecular interactions within WPUI are critical to its thermal performance. For example, enhancing interactions among SS can increase the maximum thermal decomposition temperature. Moreover, a higher imide concentration leads to stronger interactions between HS, thereby increasing the initial thermal decomposition temperature. According to morphological analysis, increasing the HS or imide content disrupts the crystallization of SS and enhances microphase separation. This increased microphase separation improves the storage modulus of WPUI at high temperatures, highlighting its superior performance under high-temperature conditions. Incorporating 5 wt% CNS into WPUI improves its EMI SE, which was found to be 50 dB, and does not negatively affect WPUI's favorable physical properties, unlike current alternatives do. These findings indicate that WPUI containing CNS is a highly promising material for multifunctional EMI shielding applications; the composite has high EMI SE, excellent thermal and mechanical properties, and an environmentally friendly production process.

Author Contributions

Chih-Lung Lin: data curation (lead), methodology (lead), project administration (lead), validation (lead), writing – original draft (lead), writing – review and editing (lead). **Yen-Yu Cheng:** data curation (equal), methodology (supporting), project administration (equal), validation (equal), writing – review and editing (supporting). **Syang-Peng Rwei:** conceptualization (supporting), funding acquisition (lead), supervision (supporting), writing – review and editing (supporting).

Acknowledgments

This study was supported by a grant from Kuroki (New Taipei City, Taiwan). This study was also financially supported by the National Science and Technology Council of Taiwan (NSTC 112-2221-E-027-005-MY2).

Conflicts of Interest

The authors declare no conflicts of interest.

Data Availability Statement

The data that support the findings of this study are available from the corresponding author upon reasonable request.

References

1. X. Chen, L. Liu, F. Pan, J. Mao, X. Xu, and T. Yan, "Microstructure, Electromagnetic Shielding Effectiveness and Mechanical Properties of Mg–Zn–Cu–Zr Alloys," *Materials Science and Engineering B* 197 (2015): 67–74, https://doi.org/10.1016/j.mseb.2015.03.012.

2. J. Zhang, J. Li, G. Tan, et al., "Thin and Flexible Fe–Si–B/Ni–Cu–P Metallic Glass Multilayer Composites for Efficient Electromagnetic Interference Shielding," *ACS Applied Materials & Interfaces* 9, no. 48 (2017): 42192–42199, https://doi.org/10.1021/acsami.7b12504.

3. K. Verstraete, L. Prévond, A.-L. Helbert, and T. Baudin, "Magnetic Shielding at Low Frequencies: Application for an Aluminum/Steel Composite Elaborated by Accumulative Roll Bonding," *Advanced Engineering Materials* 21, no. 4 (2019): 1800967, https://doi.org/10.1002/adem.201800967.

4. Y. Zhang, M. Qiu, Y. Yu, B. Wen, and L. Cheng, "A Novel Polyaniline-Coated Bagasse Fiber Composite With Core–Shell Heterostructure Provides Effective Electromagnetic Shielding Performance," *ACS Applied Materials & Interfaces* 9, no. 1 (2017): 809–818, https://doi.org/10.1021/acsami.6b11989.

5. B. Shin, S. Mondal, M. Lee, S. Kim, Y.-I. Huh, and C. Nah, "Flexible Thermoplastic Polyurethane-Carbon Nanotube Composites for Electromagnetic Interference Shielding and Thermal Management," *Chemical Engineering Journal* 418 (2021): 129282, https://doi.org/10.1016/j.cej.2021.129282.

6. L. Wang, X. Shi, J. Zhang, Y. Zhang, and J. Gu, "Lightweight and Robust rGO/Sugarcane Derived Hybrid Carbon Foams With Outstanding EMI Shielding Performance," *Journal of Materials Science and Technology* 52 (2020): 119–126, https://doi.org/10.1016/j.jmst.2020.03.029.

7. K. Wang, Q. Ma, Y. Zhang, S. Wang, and G. Han, "Ag NPs-Assisted Synthesis of Stable Cu NPs on PET Fabrics for Antibacterial and Electromagnetic Shielding Performance," *Polymers* 12, no. 4 (2020): 783, https://doi.org/10.3390/polym12040783.

8. W.-T. Cao, F.-F. Chen, Y.-J. Zhu, et al., "Binary Strengthening and Toughening of MXene/Cellulose Nanofiber Composite Paper With Nacre-Inspired Structure and Superior Electromagnetic Interference Shielding Properties," *ACS Nano* 12, no. 5 (2018): 4583–4593, https://doi.org/10.1021/acsnano.8b00997.

9. Y.-Z. Yan, K. Chen, H. R. Moon, S. S. Park, and C.-S. Ha, "Flexible and Hydrophobic Polyimide/MXene-POSS Nanocomposite Films for Electromagnetic Interference Shielding," *European Polymer Journal* 202 (2024): 112655, https://doi.org/10.1016/j.eurpolymj.2023.112655.

10. X. Li, T. Xu, W. Cao, et al., "Graphene/Carbon Fiber Network Constructed by Co-Carbonization Strategy for Functional Integrated Polyimide Composites With Enhanced Electromagnetic Shielding and Thermal Conductive Properties," *Chemical Engineering Journal* 464 (2023): 142595, https://doi.org/10.1016/j.cej.2023.142595.

11. D. Mani, M. C. Vu, S. Anand, et al., "Elongated Liquid Metal Based Self-Healing Polyurethane Composites for Tunable Thermal Conductivity and Electromagnetic Interference Shielding," *Composites Communications* 44 (2023): 101735, https://doi.org/10.1016/j.coco.2023.101735.

12. S. Yuan, T. Dai, X. Jiang, H. Zou, and P. Liu, "Transparent and Environmentally Adaptive Semi-Interpenetrating Network Hydrogels for Electromagnetic Interference Shielding," *ACS Applied Polymer Materials* 5, no. 10 (2023): 8406–8414, https://doi.org/10.1021/acsapm.3c01381.

13. A. Delavarde, G. Savin, P. Derkenne, et al., "Sustainable Polyurethanes: Toward New Cutting-Edge Opportunities," *Progress in Polymer Science* 151 (2024): 101805, https://doi.org/10.1016/j.progpolymsci.2024.101805.

14. T. Habets, F. Siragusa, B. Grignard, and C. Detrembleur, "Advancing the Synthesis of Isocyanate-Free Poly(Oxazolidones)s: Scope and Limitations," *Macromolecules* 53, no. 15 (2020): 6396–6408, https://doi.org/10.1021/acs.macromol.0c01231.

15. H. Liu and D. Sun, "Synthesis of Self-Healing Supramolecular Waterborne Polyurethane With Quadruple Hydrogen Bonds via Ureidotriazine," *Journal of Applied Polymer Science* 139, no. 15 (2022): 51932, https://doi.org/10.1002/app.51932.

16. Ł. Byczyński, M. Dutkiewicz, R. Januszewski, and S. Rojewski, "Polyurethane High-Solids Coatings Modified With Silicon-Containing Functionalized Cyclotriphosphazene," *Progress in Organic Coatings* 172 (2022): 107139, https://doi.org/10.1016/j.porgcoat.2022.107139.

17. J. Chang, H. Niu, and D. Wu, "High Performance Polyimide Fibers," in *Structure and Properties of High-Performance Fibers*, ed. G. Bhat (Sawston, Cambridge: Woodhead Publishing, 2017), 301–323, https://doi.org/10.1016/B978-0-08-100550-7.00012-7.

18. M. Lian, F. Zheng, Q. Wu, X. Lu, and Q. Lu, "Incorporating Bis-Benzimidazole Into Polyimide Chains for Effectively Improving Thermal Resistance and Dimensional Stability," *Polymer International* 69, no. 1 (2020): 93–99, https://doi.org/10.1002/pi.5922.

19. C.-L. Lin, W.-L. Lin, and S.-P. Rwei, "Synthesis and Characterization of Poly(Urethane-Imide) Derived From Structural Effect of Diisocyanates," *Journal of Polymer Research* 30, no. 2 (2023): 54, https://doi.org/10.1007/s10965-022-03408-5.

20. B. Pooladian and M. M. Alavi Nikje, "Synthesis and Characterization of Novel Water-Based Poly(Urethane-Imide) Nanodispersions," *Journal of Coatings Technology and Research* 15, no. 3 (2018): 643–647, https://doi.org/10.1007/s11998-018-0047-6.

21. R.-S. Chen, Y.-L. Cheng, and K.-W. Chang, "Synthesis and Properties of Novel Poly(Urethane-Imide) Dispersions Based on 2,2-Bis[N-(3-Hydroxyphenyl)phthalimidyl]Hexafluoropropane," *Journal of Applied Polymer Science* 111, no. 1 (2009): 517–524, https://doi.org/10.1002/app.29075.

22. K.-L. Noble, "Waterborne Polyurethanes," *Progress in Organic Coatings* 32, no. 1 (1997): 131–136, https://doi.org/10.1016/S0300-9440(97)00071-4.

23. C.-L. Lin, Y.-J. Lou, Y.-Y. Cheng, and S.-P. Rwei, "Casting Poly(Urethane-Imide) Elastomers With Improved Thermoviscoelasticity," *Journal of Applied Polymer Science* 141, no. 8 (2024): e54984, https://doi.org/10.1002/app.54984.

24. Y.-T. Hsu, W.-H. Wang, and W.-H. Hung, "Architectural Sustainability and Efficiency of Enhanced Waterproof Coating From Utilization of Waterborne Poly (Siloxane-Imide-Urethane) Copolymers on Roof Surfaces," *Sustainability* 12, no. 11 (2020): 4411, https://doi.org/10.3390/su12114411.

25. H. Honarkar, M. Barmar, and M. Barikani, "Synthesis, Characterization and Properties of Waterborne Polyurethanes Based on Two Different Ionic Centers," *Fibers and Polymers* 16, no. 4 (2015): 718–725, https://doi.org/10.1007/s12221-015-0718-1.

26. O. Pamir, N. Ocal, and F. Aydogan, "Synthesis, Characterization and Dispersion Stabilities of Novel Ionic and Nonionic Diol Modified Waterborne Polyurethane Dispersions With Different Polyols," *Journal of Dispersion Science and Technology* 44, no. 4 (2023): 585–593, https://doi.org/10.1080/01932691.2021.1956526.

27. K. Ke, Z. Sang, and I. Manas-Zloczower, "Hybrid Systems of Three-Dimensional Carbon Nanostructures With Low Dimensional Fillers for Piezoresistive Sensors," *Polymer Composites* 41, no. 2 (2020): 468–477, https://doi.org/10.1002/pc.25380.

28. M. Zhang and J. Li, "Carbon Nanotube in Different Shapes," *Materials Today* 12, no. 6 (2009): 12–18, https://doi.org/10.1016/S1369-7021(09)70176-2.

29. K. Ke, V. Solouki Bonab, D. Yuan, and I. Manas-Zloczower, "Piezoresistive Thermoplastic Polyurethane Nanocomposites With Carbon Nanostructures," *Carbon* 139 (2018): 52–58, https://doi.org/10.1016/j.carbon.2018.06.037.

30. W. M. Alvino and L. E. Edelman, "Polyimides From Diisocyanates, Dianhydrides, and Tetracarboxylic Acids," *Journal of Applied Polymer Science* 19, no. 11 (1975): 2961–2980, https://doi.org/10.1002/app.1975.070191103.

31. Y. Li and X. Huang, "Dispersion Evaluation, Processing and Tensile Properties of Carbon Nanotubes-Modified Epoxy Composites Prepared by High Pressure Homogenization," *Composites Part A: Applied Science and Manufacturing* 78 (2015): 166–173, https://doi.org/10.1016/j.compositesa.2015.08.013.

32. L. Lyu, J. Liu, H. Liu, et al., "An Overview of Electrically Conductive Polymer Nanocomposites Toward Electromagnetic Interference Shielding," *Engineered Science* 2 (2018): 26–42, https://doi.org/10.30919/es8d615.

33. H. Duan, H. Zhu, J. Gao, et al., "Asymmetric Conductive Polymer Composite Foam for Absorption Dominated Ultra-Efficient Electromagnetic Interference Shielding With Extremely Low Reflection Characteristics," *Journal of Materials Chemistry A* 8, no. 18 (2020): 9146–9159, https://doi.org/10.1039/D0TA01393E.

34. S. Anoop Kumar, A. P. Singh, P. Saini, F. Khatoon, and S. K. Dhawan, "Synthesis, Charge Transport Studies, and Microwave Shielding Behavior of Nanocomposites of Polyaniline With ti-Doped γ-Fe2O3," *Journal of Materials Science* 47, no. 5 (2012): 2461–2471, https://doi.org/10.1007/s10853-011-6068-5.

35. Y.-H. Lee, L.-Y. Wang, C.-Y. Tsai, and C.-W. Lee, "Self-Healing Nanocomposites With Carbon Nanotube/Graphene/Fe3O4 Nanoparticle Tricontinuous Networks for Electromagnetic Radiation Shielding," *ACS Applied Nano Materials* 5, no. 11 (2022): 16423–16439, https://doi.org/10.1021/acsanm.2c03492.

36. M. Peng and F. Qin, "Clarification of Basic Concepts for Electromagnetic Interference Shielding Effectiveness," *Journal of Applied Physics* 130, no. 22 (2021): 225108, https://doi.org/10.1063/5.0075019.

37. S. Tiptipakorn, W. Punuch, M. Okhawilai, and S. Rimdusit, "Property Enhancement of Polybenzoxazine Modified With Monoanhydrides and Dianhydrides," *Journal of Polymer Research* 22, no. 7 (2015): 132, https://doi.org/10.1007/s10965-015-0771-x.

38. J. Liu, D. Ma, and Z. Li, "FTIR Studies on the Compatibility of Hard–Soft Segments for Polyurethane–Imide Copolymers With Different Soft Segments," *European Polymer Journal* 38, no. 4 (2002): 661–665, https://doi.org/10.1016/S0014-3057(01)00247-6.

39. W. Zhou, D. Liu, T. Liu, L. Ni, H. Quan, and Q. Sun, "Emulsion Stability and Water Tolerance of Cationic Waterborne Polyurethane With Different Soft Segment Ratios Between Trifunctional Polyether and Bifunctional Polyester," *Materials Research Express* 6, no. 6 (2019): 065303, https://doi.org/10.1088/2053-1591/ab07f4.

40. D. H. Jung, E. Y. Kim, Y. S. Kang, and B. K. Kim, "High Solid and High Performance UV Cured Waterborne Polyurethanes," *Colloids and Surfaces A: Physicochemical and Engineering Aspects* 370, no. 1 (2010): 58–63, https://doi.org/10.1016/j.colsurfa.2010.08.046.

41. H. K. Singh, R. K. Gupta, S. K. Singh, et al., "Synthesis and Self-Assembly of Aroylhydrazone Based Polycatenars: A Structure-Property Correlation," *Journal of Molecular Liquids* 284 (2019): 282–290, https://doi.org/10.1016/j.molliq.2019.04.003.

42. Q. Tang, Y. Song, J. He, and R. Yang, "Synthesis and Characterization of Inherently Flame-Retardant and Anti-Dripping Thermoplastic Poly(Imides-Urethane)s," *Journal of Applied Polymer Science* 131, no. 18 (2014): 40801, https://doi.org/10.1002/app.40801.

43. M.-H. Tsai, S.-L. Huang, S.-J. Liu, C.-J. Chen, P.-J. Chen, and S.-H. Chen, "Synthesis and Properties of Poly(Urethane-Imide) Interpenetrating Network Membranes," *Desalination* 233, no. 1 (2008): 191–200, https://doi.org/10.1016/j.desal.2007.09.042.

44. S. Mondal and J. L. Hu, "Influence of Hard Segment on Thermal Degradation of Thermoplastic Segmented Polyurethane for Textile Coating Application," *Polymer-Plastics Technology and Engineering* 46, no. 1 (2007): 37–41, https://doi.org/10.1080/03602550600948715.

45. T.-L. Wang and T.-H. Hsieh, "Effect of Polyol Structure and Molecular Weight on the Thermal Stability of Segmented Poly(Urethaneureas)," *Polymer Degradation and Stability* 55, no. 1 (1997): 95–102, https://doi.org/10.1016/S0141-3910(96)00130-9.

46. K. A. Barrera-Rivera, L. Peponi, Á. Marcos-Fernández, J. M. Kenny, and A. Martínez-Richa, "Synthesis, Characterization and Hydrolytic Degradation of Polyester-Urethanes Obtained by Lipase Biocatalysis," *Polymer Degradation and Stability* 108 (2014): 188–194, https://doi.org/10.1016/j.polymdegradstab.2014.04.004.

47. Q. Tang, Q. Ai, J. He, X. Li, and R. Yang, "Synthesis and Characterization of Thermally Stable Poly(Urethane–Imide)s Based on Novel Diols-Containing Imide and Alkynyl Groups," *High Performance Polymers* 25, no. 7 (2013): 798–812, https://doi.org/10.1177/0954008313486280.

48. Y. Xiao, L. Jiang, Z. Liu, et al., "Effect of Phase Separation on the Crystallization of Soft Segments of Green Waterborne Polyurethanes,"

Polymer Testing 60 (2017): 160–165, https://doi.org/10.1016/j.polymertesting.2017.03.029.

49. M. M. Mirhosseini, V. Haddadi-Asl, and I. S. Jouibari, "A Simple and Versatile Method to Tailor Physicochemical Properties of Thermoplastic Polyurethane Elastomers by Using Novel Mixed Soft Segments," *Materials Research Express* 6, no. 6 (2019): 065314, https://doi.org/10.1088/2053-1591/ab0cba.

50. Y. Gao, J. Lv, L. Liu, and Y. Yu, "Effect of Diacylhydrazine as Chain Extender on Microphase Separation and Performance of Energetic Polyurethane Elastomer," *E-Polymers* 20, no. 1 (2020): 469–481, https://doi.org/10.1515/epoly-2020-0052.

51. P. L. Jagadeshvaran, K. Panwar, I. Ramakrishnan, and S. Bose, "Solvent-Free Conductive Coatings Containing Chemically Coupled Particles for Functional Textiles," *ACS Applied Electronic Materials* 3, no. 12 (2021): 5402–5414, https://doi.org/10.1021/acsaelm.1c00874.